RSC Advances

PAPER

View Article Online
View Journal | View Issue

Cite this: *RSC Adv.*, 2025, **15**, 4619

Hierarchical nanoporous NiCoN nanoflowers with highly rough surface electrode material for high-performance asymmetric supercapacitors†

Mohan Reddy Pallavolu,*[a] Chandu V. V. Muralee Gopi,[b] Samikannu Prabu,[c] Punna Reddy Ullapu,[d] Jae Hak Jung,*[a] Sang Woo Joo*[e] and R. Ramesh*[f]

This study presents a novel strategy to enhance the energy storage performance of asymmetric supercapacitors (ASCs) by utilizing nanoporous NiCoN flower structures as the positive electrode material. The NiCoN material is synthesized *via* a straightforward hydrothermal method, followed by calcination in a nitrogen atmosphere. The resulting electrode demonstrates exceptional electrochemical properties, including a high specific capacity of 773 C g^{-1} (1955 F g^{-1}), excellent rate capability, and outstanding cycling stability. The hierarchical architecture of the NiCoN electrode, composed of interconnected porous nanosheets, facilitates efficient charge transfer and enhanced electrolyte ion diffusion. When paired with activated carbon (AC) as the negative electrode in the NiCoN//AC ASC configuration, the device achieves an impressive energy density of 36 W h kg^{-1} at a power density of 775 W kg^{-1}. Moreover, the device exhibits remarkable cycling stability, retaining 85% of its initial capacitance after 5000 charge–discharge cycles. These findings underscore the potential of NiCoN as a high-performance electrode material for ASCs, offering a promising pathway for advancements in next-generation energy storage technologies.

Received 30th October 2024
Accepted 25th December 2024

DOI: 10.1039/d4ra07757a

rsc.li/rsc-advances

1. Introduction

As renewable energy sources continue to gain momentum, the demand for reliable and efficient energy storage solutions is rapidly increasing.[1,2] Although lithium-ion batteries (LIBs) currently dominate the market, they face several limitations, including energy density constraints, safety concerns related to electrolyte flammability, and performance degradation due to dendrite formation.[3,4] These challenges necessitate the exploration of alternative energy storage technologies. On the other hand, electrochemical capacitors, often referred to as ultracapacitors or supercapacitors (SCs), have garnered significant interest due to their advantageous properties, including ease of manufacturing, rapid charge, and discharge capabilities, long service life, and simple operating mechanisms.[5–7] However, while SCs excel in power density, their relatively low energy density limits their applicability in certain applications.[8]

Significant research has been dedicated to improving SC energy density to make them more competitive with lithium-ion batteries. Two primary strategies emerged in this effort: expanding the voltage window and enhancing capacitance.[9] Despite their voltage potential, organic solvents pose safety risks, limiting their practical application.[10] On the other hand, aqueous asymmetric supercapacitors, which use activated carbon and transition metal oxides, present a promising alternative due to their wider voltage window and the combination of capacitive and faradaic storage mechanisms.[11] Also, the morphological characteristics of the electrode material play a significant role in influencing its capacitance, making the selection of electrode material a key factor in optimizing energy storage performance.[12]

Recently, binary transition metal oxides (BTMOs) have gained significant attention as electrode materials for supercapacitors. Their ability to exist in multiple oxidation states, combined with enhanced conductivity and favorable electrochemical properties, positions them as promising candidates for high-performance energy storage devices.[13,14] BTMOs offer advantages over single metal oxides, such as improved charge storage capacity and faster charge–discharge rates, making them valuable for applications requiring high power density and long-term durability.[15]

[a]*School of Chemical Engineering, Yeungnam University, Gyeongsan 38541, Republic of Korea. E-mail: pmreddy@yu.ac.kr; jhjung@ynu.ac.kr*

[b]*Department of Electrical Engineering, University of Sharjah, P.O. Box 27272, Sharjah, United Arab Emirates*

[c]*Graduate Institute of Environmental Engineering, National Central University, Zhong-Da Road, Zhong-Li District, Tao-Yuan City, Taiwan*

[d]*School of Science and Technology (UST), 176 Gajung-dong, 217 Gajungro, Yuseong-gu, Daejung 305-333, South Korea*

[e]*School of Mechanical Engineering, Yeungnam University, Gyeongsan 38541, Republic of Korea. E-mail: swjoo@yu.ac.kr*

[f]*Department of Chemical Engineering, School of Mechanical, Chemical and Materials Engineering, Adama Science and Technology University, P.O. Box 1888, Adama, Ethiopia. E-mail: ramesh.redrouthu@astu.edu.et*

† Electronic supplementary information (ESI) available. See DOI: https://doi.org/10.1039/d4ra07757a

However, metal oxide-based electrodes often suffer from limited electrical conductivity, which negatively impacts their overall electrochemical performance.[16] While advancements have been made in this area, the inherent limitations of metal oxides, such as poor stability and conductivity, persist. In contrast, binary metal nitrides – materials composed of two different metal elements combined with nitrogen – have emerged as promising candidates for supercapacitor electrodes. These nitrides exhibit high electronic conductivity, excellent cycling stability, and fast charge–discharge rates, making them attractive for energy storage applications.[17] The combination of two metal elements in binary nitrides results in synergistic effects that enhance their electrochemical performance, such as improved capacitance, rate capability, and energy density. Among binary metal nitrides, cobalt and nickel nitrides have shown particular promise due to their high reactivity and favorable electrochemical properties.[18,19] These materials have been extensively studied for their potential applications in supercapacitors, with research focusing on optimizing their synthesis methods, electrode fabrication techniques, and operating conditions to achieve the desired performance characteristics. Some examples consisting of Ni–Mo oxide precursor was annealed to make $Ni_{0.2}Mo_{0.8}N$ nanorods in the presence of NH_3, where the Ni nanoparticles were decorated on the nanorods. The $Ni_{0.2}Mo_{0.8}N$ electrode material showed high power and energy densities.[20] Li *et al.*, made honeycomb-like CoN–Ni_3N/NC nanosheets using a solvothermal technique and treated them in the NH_3 atmosphere.[21] The CoN–Ni_3N/NC electrode exhibited better electrochemical performance by increasing of active site and conductivity. Liu *et al.* synthesized Ni-doped Co–Co_2N heterostructures that were grown by a metal–organic framework and delivered high specific capacities.[22] This literature confirms the remarkable electrochemical performance of binary nitrides.

Interestingly, NiCoN, a binary metal nitride composed of nickel, cobalt, and nitrogen, has recently emerged as a highly promising electrode material for supercapacitors, offering exceptional electrochemical performances. The synergistic interaction between nickel and cobalt, coupled with the presence of nitrogen, improves electrical conductivity, reduces energy losses, and enhances overall capacitance and stability. Recent studies have highlighted the potential of NiCoN in supercapacitor applications. For instance, Liu *et al.* synthesized NiCoN nanosheets on graphene paper, achieving high specific surface area and excellent electrochemical performance, including a high specific capacitance of 960 F g^{-1} and 95% cycling stability after 5000 cycles.[23] Similarly, Gao *et al.* reported a specific capacitance of 1484 mF cm^{-2} for NiCoN nanostructures using supercapacitors.[24] These findings highlight the potential of NiCoN as a promising electrode material for supercapacitor applications. However, a significant challenge remains in growing transition metal nitrides due to the high nitration temperatures required. The final morphology and distribution of active sites may be influenced by the various preparation methods used, such as solvothermal synthesis, NH_3 annealing, and MOF-assisted growth.

In the present work, we fabricated nanoporous NiCoN flower-like structures through nitrogen treatment of NiCo bimetal carbonate hydroxides without affecting the structural morphology. The novelty of the present work lies in the fabrication of nanoporous NiCoN flower-like structures *via* a nitrogen treatment of NiCo bimetal carbonate hydroxides, which successfully maintains the ordered nanosheet arrangement on nickel foam. This structural design enhances electron transfer within the electrode, addressing a key challenge in energy storage materials. Additionally, the application of the NiCoN structure as an anode in an asymmetric supercapacitor (ASC) with activated carbon as the cathode demonstrates superior energy density (36 W h kg^{-1} at 775 W kg^{-1} power density) and exceptional cycling stability (85% capacitance retention after 5000 cycles), outperforming many previously reported ASCs. This work highlights an innovative approach to developing high-performance, durable electrodes for advanced energy storage systems.

2. Experimental

2.1. Materials

Nickel nitrate hexahydrate ($Ni(NO_3)_2 \cdot 6H_2O$), cobalt nitrate hexahydrate ($Co(NO_3)_2 \cdot 6H_2O$), ammonium floride (NH_4F), and urea (CH_4N_2O) were purchased from Sigma Aldrich, Korea. Ni foam was purchased in MTI, Korea. Polyvinylidene fluoride, carbon black (Denka black), *N*-methyl-2 pyrrolidone (NMP), ethanol, and hydrochloric acid (HCl) were provided by the Daejung Chemicals.

2.2. Preparation of flower-like nanoporous NiCoN electrode material

The flower-like NiCoN with a highly rough surface was synthesized, as illustrated in Fig. 1. A solution containing 1 mmol of $Ni(NO_3)_2 \cdot 6H_2O$ and 1 mmol of $Co(NO_3)_2 \cdot 6H_2O$ was prepared in 30 mL of deionized water and stirred magnetically for 30 min. Subsequently, 5 mmol of NH_4F and 10 mmol of urea were added sequentially to the solution. The mixture was heated in a sealed autoclave at 120 °C for 6 h and then cooled to room temperature naturally. The precipitate from the hydrothermal reaction was collected and washed repeatedly with deionized water. The collected powder was then calcined at 500 °C for 2 h in a tube furnace under a nitrogen gas flow. To test the electrochemical performance of prepared NiCoN material, initially, Ni foam (NF) (2×1 cm^2) was cut into pieces for conducting substrate, which was cleaned with 3 M HCl and water then ethanol for each 10 min. The NF thickness was 1.6 mm. The slurry was prepared using drop-casting to coat on NF with a working area of 1×1 cm^2 for electrode preparation. By mixing active material, PVDF, and carbon black in the ratio of 80 : 10 : 10 while grinding with adding NMP, a slurry was made. The coated NFs were dried in an oven at 75 °C overnight to remove the NMP solution and other counterparts. The coated NF had a mass loading of approximately 2.3 mg.

2.3. Material characterization

We utilized a combination of characterization techniques to elucidate the synthesized electrodes' structural and

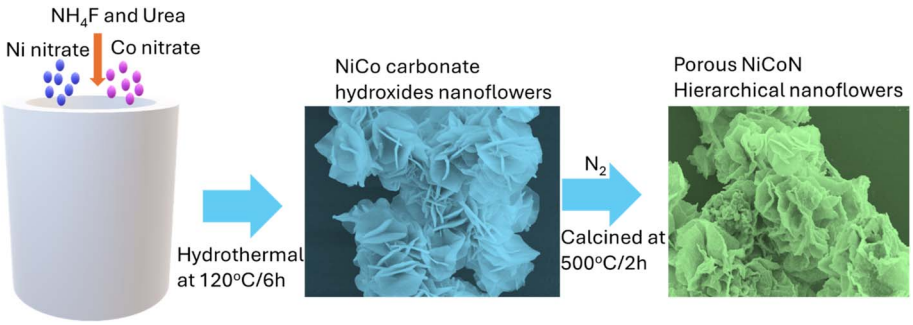

Fig. 1 Schematic of synthesis hierarchical NiCoN porous nanoflower-sheets.

compositional properties. Scanning electron microscopy (SEM, S4800, Hitachi), transmission electron microscopy (TEM, Technai G^2 STwin), and X-ray photoelectron spectrometer (XPS, K-alpha, thermoscientific) were employed to examine the morphology, microstructure, and composition of the fabricated materials, respectively. X-ray diffraction (XRD, PANalytical Xpert Pro) analysis confirmed the crystalline structure and phase purity, while Fourier transform infrared (FTIR, model Spectrum100, PerkinElmer) spectroscopy provided information about the chemical composition and functional groups in the materials.

2.4. Electrochemical measurements

An electrochemical workstation (Bio-Logic VMP-3e) was employed in a three-electrode configuration to assess the electrochemical properties of the electrodes. Cyclic voltammetry (CV), galvanostatic charge–discharge (GCD), and electrochemical impedance spectroscopy (EIS) techniques were utilized in a cell containing a 3 M KOH electrolyte solution. The fabricated NiCoN electrode served as the working electrode, while an Ag/AgCl electrode acted as the reference electrode and a platinum wire was used as the counter electrode. The specific capacitance (C_S) of the electrodes was calculated from the GCD curves using the following equation:

$$C_S = \frac{I \times \Delta t}{\Delta V \times m} \quad (1)$$

where I represents the discharge current, ΔV denotes the potential window during discharge, Δt is the discharge time, and m is the mass of the active electrode material.

Before fabricating an ASC, the charge stored in the positive and negative electrodes must be balanced to ensure optimal performance. This balance can be achieved by ensuring that the following equation holds:

$$\frac{m_+}{m_-} = \frac{C_- \times \Delta V_-}{C_+ \times \Delta V_+} \quad (2)$$

where m, ΔV, and C represent the respective electrodes' mass, potential window, and specific capacitance.

An ASC was assembled using NiCoN-loaded Ni foam as the positive electrode, AC as the negative electrode, a cellulose paper separator, and a 3 M KOH electrolyte. The specific capacitance (C_{SC}, F g^{-1}), energy density (E, W h kg^{-1}), and power density (P, W kg^{-1}) of the ASC were calculated from the GCD curve using the following equations:

$$C_{SC} = \frac{I \times \Delta t}{\Delta V \times M} \quad (3)$$

$$E = \frac{C_{SC} \times \Delta V^2}{7.2} \quad (4)$$

$$P = \frac{3600 \times E}{\Delta t} \quad (5)$$

where I, Δt, ΔV, and M have their usual meanings.

3. Results and discussion

The formation of NiCoN is synthesized by the two-step process, as presented schematically in Fig. 1. In the first step, NiCo bimetal carbonate hydroxides were formed in the hydrothermal method, and then the resulting product was calcined in the N_2 atmosphere to attain NiCoN nanostructured material. In this synthesis, urea is utilized as a precipitating agent, while NH_4F acts as a surfactant to control the morphology of the final product. Initially, Ni^{2+} and Co^{2+} ions form metal salt complexes with F from NH_4F in the homogeneous solution. As the temperature rises, urea undergoes hydrolysis-precipitation, releasing Ni^{2+} and Co^{2+} ions that react with CO_3^{2-} and OH^- derived from urea decomposition to create NiCo bimetal carbonate hydroxides. After calcination in N_2, the metal oxide product was then formed as NiCoN nanostructured material. The reaction mechanism of the synthesis is provided below.[25]

$$CH_4N_2O + H_2O \rightarrow 2\,NH_3 + CO_2$$

$$NH_3 + H_2O \rightarrow NH_4OH$$

$$NH_4OH \rightarrow NH^{4+} + OH^-$$

$$CO_2 + OH^- \rightarrow HCO_3^- \rightarrow H^+ + CO_3^{2-}$$

$$2Ni^{2+} + CO_3^{2-} + 2OH^- \rightarrow Ni_2(CO_3)(OH)_2$$

$$2Co^{2+} + CO_3^{2-} + 2OH^- \rightarrow Co_2(CO_3)(OH)_2$$

$$Ni_2(CO_3)(OH)_2 + Co_2(CO_3)(OH)_2 + N_2 \rightarrow 2NiCoN + 2CO_2 + 2H_2O$$

X-ray diffraction (XRD) analysis was conducted on the as-prepared NiCo bimetal carbonate hydroxides and NiCoN powder to confirm the formation of nickel and cobalt nitride phases after calcining with N_2. The characteristic XRD peaks belonging to the nickel and cobalt nitrate, as shown in Fig. 2a, indicate the successful synthesis of NiCoN. From the XRD, the XRD of NiCo carbonate hydroxide shows peaks at 11.5, 33.2, and 59.5°, belonging to the Co and Ni carbonate hydroxides (JCPDS (Ni) 35-0501 and (Co) 48-0083), which are well consistent with the literature.[26,27] The high intense XRD of NiCoN sample peaks positioned at 2θ values of 36.72°, 42.64°, 44.34°, 51.7°, and 61.8° correspond to the polycrystalline hexagonal Co_3N (JCPDS card no. 06-0691) and Ni_3N or $Ni_{3-x}Co_xN$ (JCPDS card no. 10-0280) phases, confirming the transformation of the transition metal precursors into metal nitrides.[28,29] Most of the peak positions of Co_3N or Ni_3N demonstrate a similar position due to the similar atomic sizes of Ni and Co. FTIR spectroscopy was also performed to identify the functional groups in the samples. The NiCo carbonate hydroxide samples show FTIR peaks at 509 and 633 cm^{-1} are associated with bending and stretching vibrations of metal (Ni/Co)–O–N bonds.[30] These vibrations indicate interactions between nickel or cobalt, oxygen, and nitrogen within the sample structure. A broad peak at 3484 cm^{-1} is associated with metal-OH stretching vibrations.[31] Peaks at 1603 and 1696 cm^{-1} are attributed to N=H and C=N bonds, respectively, while the peak at 1338 is assigned to N–O bonds.[32–34] Further, the N_2 calcined sample (NiCoN) shows two high intense peaks at 534 and 642 cm^{-1} are attributed to the metal–N–O, and metal–N bonds.[35] The XRD and FTIR results provide crucial insights into the complex chemical environment of the NiCoN sample, emphasizing the coexistence of M–N and M–O phases. The XRD patterns likely reveal distinct diffraction peaks corresponding to both nitride and oxide crystalline structures, indicating their simultaneous presence within the material. This dual-phase nature is significant as M–Ns contribute to enhanced electrical conductivity and catalytic activity, while M–Os offer robust stability and strong redox activity. FTIR spectra further corroborate this by displaying characteristic vibrational modes associated with metal–nitride (*e.g.*, M–N stretching) and metal–oxide (*e.g.*, M–O stretching) bonds, highlighting the synergy between these phases. This coexistence creates a unique chemical and electronic environment that facilitates efficient charge transfer and active site availability, directly improving the electrochemical performance, including higher catalytic efficiency, prolonged stability, and superior reactivity in applications like energy storage.

The elemental composition and purity of the NiCoN electrode were analyzed using XPS. As shown in Fig. 2c, the XPS spectrum confirms the presence of Ni, Co, and N elements in the NiCoN material, indicating successful synthesis of NiCoN. High-resolution XPS spectra provide deeper insights into the chemical states of the respective elements, which are crucial for understanding the material's electrochemical performance. The deconvoluted Co 2p spectrum presented in Fig. 2d reveals a pair of spin–orbit doublets, with peaks at approximately 779.2 and 796.4 eV corresponding to Co^{3+}, and peaks at 781.8 and 798.1 eV corresponding to Co^{2+} oxidation states.[36] Similarly, the high-resolution Ni 2p spectrum in Fig. 2e shows two spin–orbit

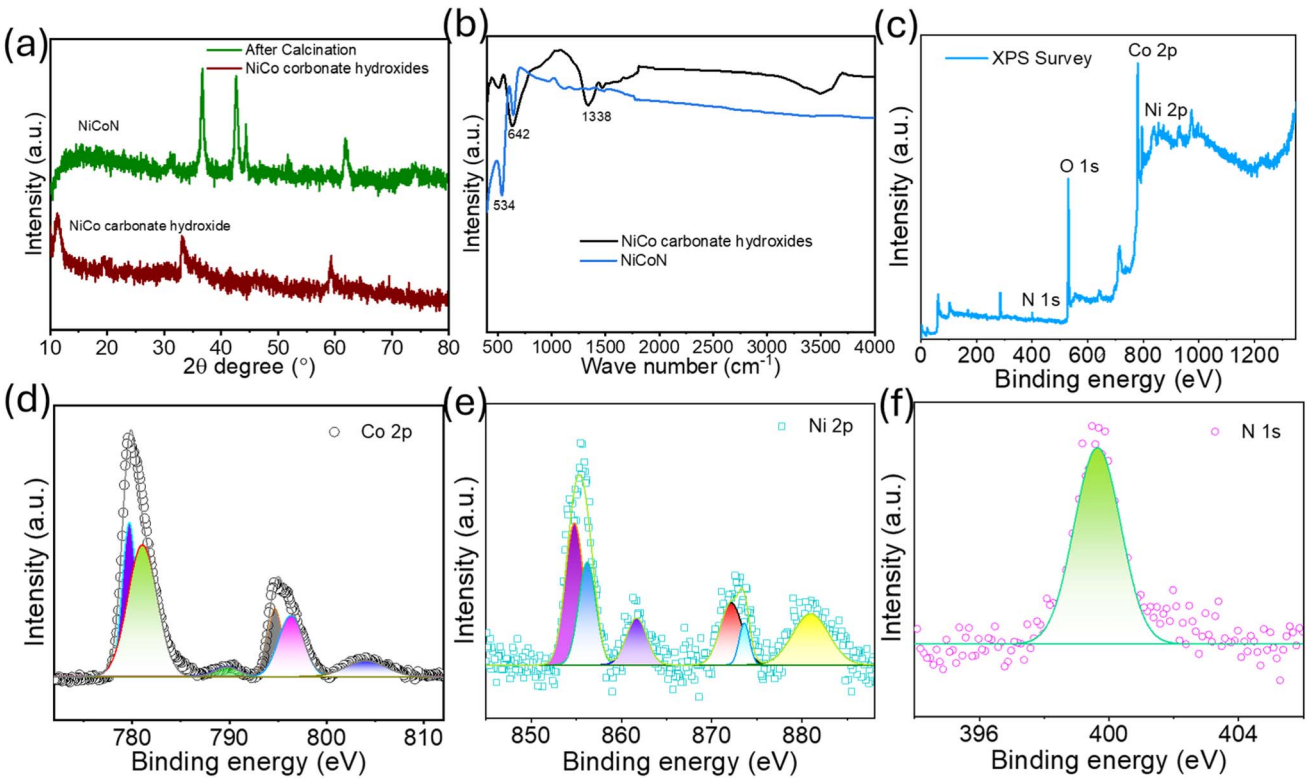

Fig. 2 (a) XRD pattern, (b) FTIR spectra, (c) XPS spectrum, and (d–f) high-resolution XPS analysis of the NiCoN electrode on Ni foam surface.

peak pairs, corresponding to Ni^{3+} and Ni^{2+} states. The fitting peaks located at 856.2 and 873.6 eV are attributed to Ni^{3+}, while the other two peaks at 854.6 and 872.5 eV indicate Ni^{2+}.[37] Additionally, two shake-up satellite peaks were observed in the Ni 2p spectrum. The coexistence of Co^{2+} and Ni^{2+} oxidation states is significant, which enhances the redox activity, contributing to improved charge storage capability in supercapacitors. The existence of different oxidation states suggests that the NiCoN structure is well developed and has a strong, active surface for redox reactions. The presence of shake-up satellite peaks indicates there are significant interactions with the surrounding ligands, providing additional evidence for the formation of a mixed metal nitride structure. The N 1s XPS spectrum in Fig. 3f shows a prominent peak at 399.6 eV, attributed to N species, confirming the formation of metal nitrides.[38] This finding is significant, as the incorporation of nitrides into the NiCoN sample is known to enhance electrical conductivity and catalytic activity, key factors for improving overall electrochemical performance. The introduction of nitrogen into the structure not only facilitates charge transport but also contributes to structural stability, ensuring the material retains its integrity during extended cycling. This stability is crucial for confirming the electrode's long operational lifespan in practical applications. Additionally, the intense oxidation peak observed in the analysis can be attributed to the formation of Ni–O and Co–O bonds, likely due to air exposure during sample preparation and storage. These oxide species may also contribute to the material's electrochemical behavior by adding redox-active sites, further complementing the nitrides in boosting performance. This dual-phase synergy highlights the potential of NiCoN as a robust and efficient electrode material.[39]

The morphological characteristics of the synthesized samples were examined using SEM. Fig. 3a–c presents SEM images of the NiCoN heterostructures at different magnifications. The SEM images reveal a nanoporous, flower-like structure composed of highly rough nanosheets. These nanosheets were firmly interconnected, facilitating efficient charge transfer between the active components of NiCoN and the current collector. The loosely arranged nanostructures along with abundant interconnected open spaces, clearly indicate a large electroactive surface area, which is beneficial for enhancing the electrode's electrochemical performance. Additionally, energy-dispersive X-ray spectroscopy (EDS) analysis was performed to investigate the elemental composition and distribution within the NiCoN material. The EDS spectrum, as shown in Fig. 3d, confirms the presence of Ni, Co, and Ni atoms within the synthesized material. EDS mapping images (Fig. 3e–g) further demonstrate the uniform distribution of these elements throughout the NiCoN electrodes, underscoring the homogeneity of the material. Furthermore, the morphological and crystalline characteristics of the NiCoN electrodes were analyzed using TEM and high-resolution TEM (HR-TEM). The TEM images in Fig. 3h and i depict the hierarchical, flower-like structure composed of porous nanosheets, which aligns with the SEM observations. The measured *d*-spacing of 0.22 nm corresponds to the (002) crystal planes of NiCoN, as confirmed through detailed analysis (Fig. 3j). The selected area electron diffraction (SAED) pattern in Fig. 3k displays a series of well-defined concentric rings, confirming the polycrystalline

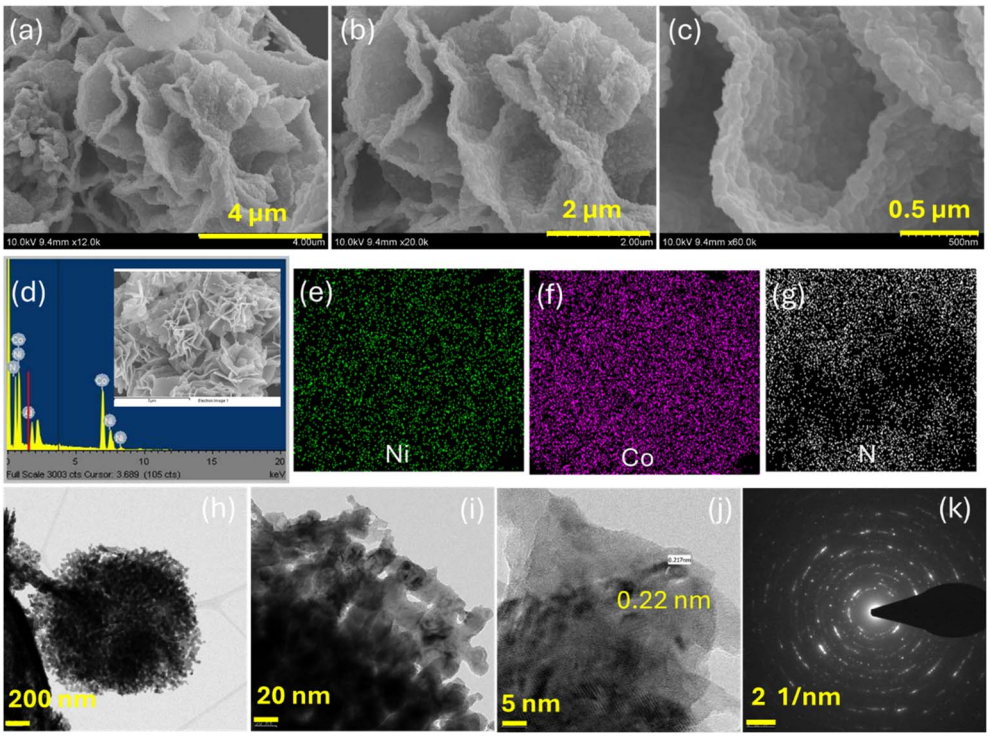

Fig. 3 (a–c) SEM, (d) EDS spectrum, (e–g) EDS mapping images, (h) TEM, (j) HR-TEM, and (k) SAED pattern of as-prepared NiCoN electrode.

nature of the NiCoN material. These diffraction rings were precisely indexed to the (220), (311), (110), (002), and (101) planes, aligning with the expected crystal structure of NiCoN. The clear and sharp nature of these rings indicates high crystallinity, which is crucial for optimizing material properties. This polycrystalline structure ensures efficient charge transport pathways, enhanced electronic conductivity, and a higher density of active sites for energy storage. The crystalline quality thus plays a pivotal role in the superior performance and reliability of NiCoN-based supercapacitor electrodes.

Fig. 4a displays CV curves of NiCoN at scan rates ranging from 3 to 12 mV s^{-1} within a potential window of 0 to 0.5 V (*vs.* Ag/AgCl). For the increased scan rates, well-defined redox peaks are evident, which confirms typical pseudocapacitive behavior characterized by rapid charge transfer kinetics. These redox peaks are primarily attributed to faradaic reactions involving the oxidation and reduction of M–O/M–O–OH species (where M represents Ni or Co).[40] As the scan rate increases, the anodic and cathodic peaks shift due to polarization effects within the electrode material.[41] The suitability of NiCoN as an electrode material for energy storage applications was further evaluated using galvanostatic charge–discharge (GCD) measurements. The GCD tests were performed over a potential range of 0 to 0.4 V (*vs.* Ag/AgCl) at current densities ranging from 1 to 10 A g^{-1}, as shown in Fig. 4b. The resulting potential–time profiles demonstrate excellent symmetry at all current densities, indicating highly reversible redox reactions, low polarization, and high coulombic efficiency. These findings align with the CV results, suggesting strong pseudocapacitive behaviour. Fig. 4c presents the specific capacitance values of NiCoN calculated from the GCD curves. The NiCoN electrode exhibited excellent pseudocapacitive performance, delivering specific capacities (specific capacitance) of 773 (1955), 584 (1537), 454 (1219), 350 (959), 280 (789), and 220 (629 F g^{-1}) C g^{-1} at current densities of 1, 2, 3, 5, 7, and 10 A g^{-1}, respectively. These results suggest that high specific capacity is due to the rich redox reactions occurring during the oxidation and reduction processes. The rate capability of the NiCoN electrode is 32.2%.

Fig. 4d presents Nyquist plots of the NiCoN electrode before and after cycling. These plots were obtained by measuring the electrochemical impedance within a 100 kHz to 0.01 Hz frequency range. The Nyquist plots display small semicircles at high frequencies, which indicate charge transfer resistance (R_{ct}), and slopping lines at lower frequencies, which represent Warburg impedance, reflecting ion diffusion behavior. The initial intersection of the Nyquist plot with the real axis at high frequencies corresponds to the solution resistance (R_S) of the electrode material. Further, using the equivalent circuit, EIS data was fitted and correlated with the experimental results. The calculated R_S (0.7 Ω) values remained virtually unchanged before and after cycling, indicating the better supercapacitive performance with stable electrochemical stability of the electrode. The R_{ct} values were determined to be 1.1 Ω before cycling and 2.1 Ω after cycling, reflecting a slight increase and demonstrating good supercapacitive performance. In addition, the slope of the low-frequency region was approximately 45–75°, indicating the electrochemical results occur from diffusion and surface-controlled processes, corroborating with the CV results. These EIS findings highlight the high conductivity and efficient electrolyte ion transport of the NiCoN electrode. The long-term

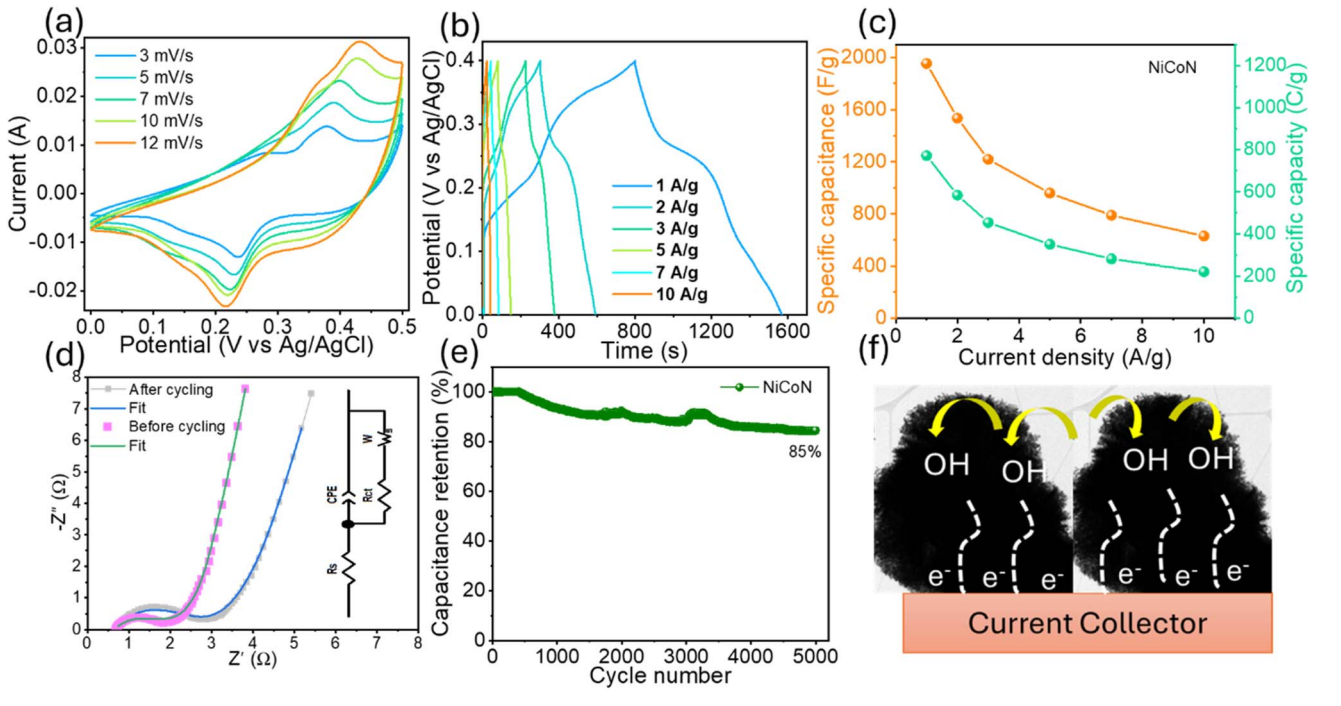

Fig. 4 (a) CV curves, (b) GCD plots, and (c) specific capacitance and specific capacity values of the NiCoN electrode. (d) EIS analysis of the NiCoN electrode before and after cycling. (e) Cycling stability of the NiCoN electrode. (f) A schematic representation of the charge transfer mechanism between the NiCoN electrode and the electrolyte.

cycling stability of the NiCoN electrode was assessed through GCD tests at a current density of 6 A g^{-1}, as shown in Fig. 4e. The NiCoN electrode maintained 85% of its initial specific capacitance after 5000 cycles, demonstrating excellent long-term durability. The gradual decline in specific capacity can be attributed to the loss of active sites due to repeated charging and discharging cycles.[42] Finally, Fig. 4f illustrates the charge transfer mechanism between the NiCoN electrode and the electrolyte. The growth of NiCoN nanoporous flower structures facilitates the efficient electrolyte ions transport. Additionally, the hierarchical nanoporous flower structures offer numerous electroactive sites, contributing to high capacity. Remarkably, the nanosheet morphology of the NiCoN nanoflowers effectively shortens the diffusion pathways for electrolyte ions, facilitating faster ion transport. This structural feature enhances the overall energy storage performance by improving the material's ion accessibility and charge/discharge kinetics, leading to higher efficiency and capacity in supercapacitor applications.

Further, asymmetric supercapacitor (ASC) devices are designed to examine the advantages of the specific electrode material properties to enhance energy and power densities with wider operating voltage window.[43,44] To demonstrate the practical electrochemical capabilities of the NiCoN electrode material, we constructed an ASC device. The device employed NiCoN as the positive electrode, activated carbon as the negative electrode, a cellulose paper separator, and a KOH aqueous electrolyte (Fig. 5a). The electrochemical performance data of the activated carbon is provided in the ESI† and the negative electrode exhibits the specific capacitance of 229 F g^{-1} at 1 A g^{-1} current density. To optimize energy density and ensure charge balance, the mass ratio of the positive electrode (NiCoN) to the negative electrode (activated carbon) was adjusted to

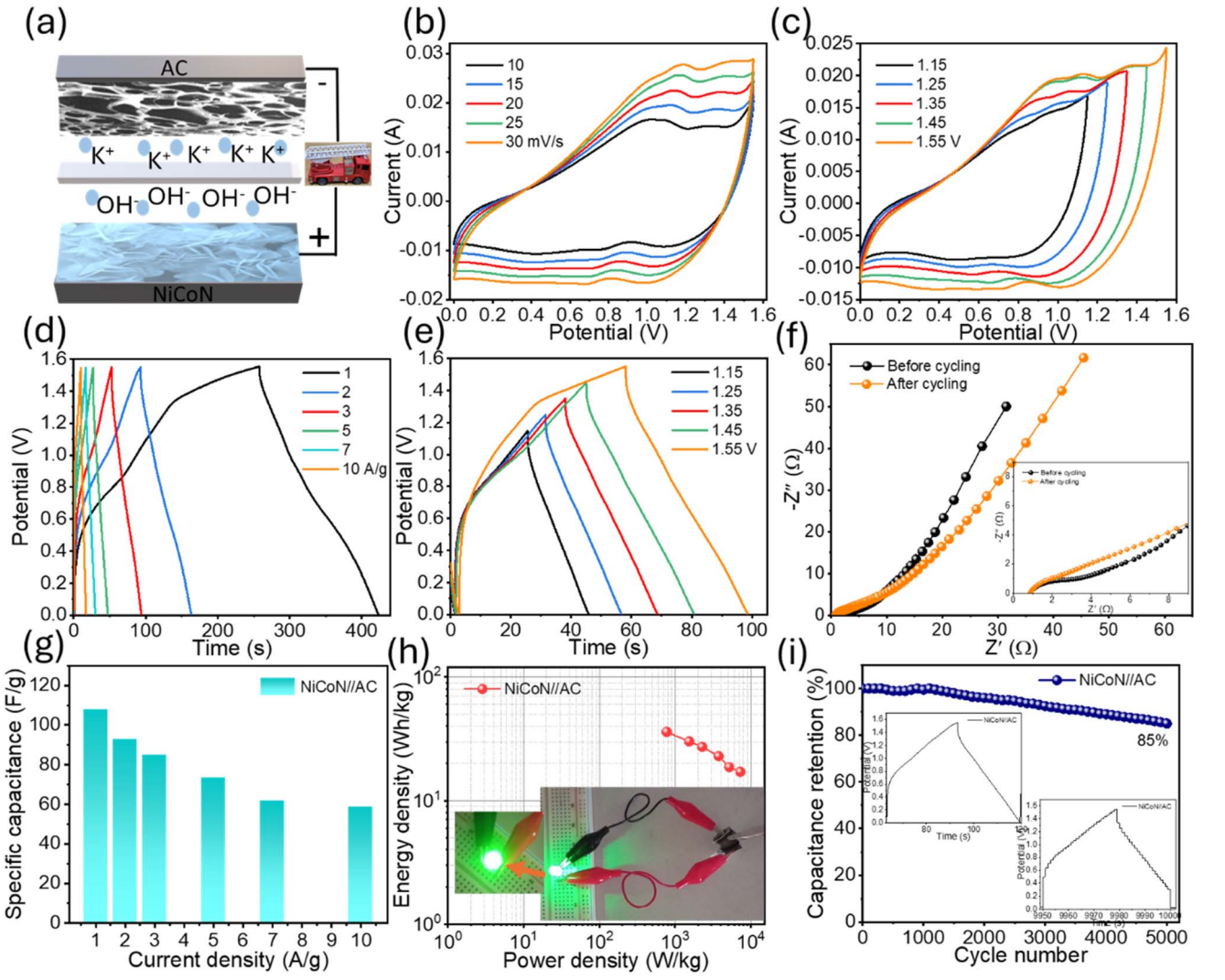

Fig. 5 (a) Schematic representation of the NiCoN//AC ASC device. (b) CV curves of the ASC device at different scan rates. (c) CV curves of the ASC device at various potential windows. (d) GCD curves of the ASC device at different current densities. (e) GCD curves of the ASC device at various potential ranges. (f) Nyquist plot of the ASC device before and after cycling. (g) Specific capacitance values and (h) Ragone plot of the assembled ASC device. (i) The cycling performance of the ASC device is over 5000 cycles, with an inset showing the GCD curves of the first and last cycles for comparison.

approximately 3.5. Fig. 5b presents the CVs of the NiCoN//AC ASC device, recorded at various scan rates ranging from 10 to 30 mV s^{-1}. The CV curves exhibit a pseudo-rectangular shape, reflecting contributions from both electrochemical (faradaic) and electrostatic reaction processes to the overall charge storage.[45] The increasing area under the CV curves at higher scan rates signifies efficient ion diffusion and enhanced electrochemical/electrostatic reactions.[46] Importantly, the CV profiles maintained their shape as scan rates increased, indicating minimal resistance to electron transfer, essential for high-performance charge storage.[47] To explore the ASC device's operational voltage window, CV measurements were performed at various potential windows at a constant scan rate (Fig. 5c), revealing stable electrochemical performance within a 0 to 1.55 V voltage range.

Fig. 5d illustrates the GCD plots of the NiCoN//AC ASC device, measured at current densities ranging from 1 to 10 A g^{-1}. The absence of voltage plateaus during discharge indicates that the device operates through supercapacitive or pseudocapacitive mechanisms.[45] Additionally, the minimal iR drop observed at the beginning of the discharge process at all current densities indicates low internal resistance and efficient electron transfer within the device.[48] Fig. 5e shows the GCD plots of the ASC device at different operating voltages and a constant current density of 3 A g^{-1}, where the device achieved the longest charge–discharge times at 1.55 V. The non-ideal, sloping discharge profiles reflect the pseudocapacitive nature of the electrode material. The EIS analysis of the ASC device was conducted before and after cycling measurements, as illustrated in Fig. 5f. The EIS spectra of the device exhibited minor variations before and after the cycling test, confirming its desired stability. The ASC exhibited exceptional rate capability, with a specific capacitance of 108 F g^{-1} at 1 A g^{-1} and 59 F g^{-1} even at 10 A g^{-1}, maintaining 55% of its capacitance rate capacitance at higher current densities, as evidenced by the GCD results shown in Fig. 5g. A Ragone plot (Fig. 5h), summarizes the energy and power densities of the ASC device. The device achieved a energy density of 36 W h kg^{-1} at a power density of 775 W kg^{-1}. Even at a higher power density of 7250 W kg^{-1}, the ASC maintained an energy density of 17.1 W h kg^{-1}. These results are compared with the previous literature on energy and power densities and the tabulated values are stated in Table S1.† The practical viability of the ASC device demonstrated by its ability to power a commercially available green LED bulb, as shown in the inset of Fig. 5h, which remained illuminated for an extended period. The cycling stability of the device is essential for practical applications. Fig. 5i shows the long-term cycling performance at a current density of 4 A g^{-1}. Remarkably, the ASC device retained 85% of its initial capacitance after 5000 cycles, indicating exceptional cycling stability and high reversibility. The inset of Fig. 5i compares the GCD curves from the 1st and 5000th cycles, further supporting its long-term durability.

In summary, NiCoN has proven to be an outstanding anode material for supercapacitors, offering exceptional potential for enhancing energy storage capabilities. This innovative approach introduces a promising direction for the development of advanced ASCs, which could substantially improve energy density and extended storage duration, advancing supercapacitor technology to meet real-world energy storage demands.

4. Conclusions

This study successfully presents the development of a novel NiCoN electrode material for ASCs, showcasing its promising potential for energy storage applications. The NiCoN electrode, featuring a unique nanoporous flower-like structure, demonstrated superior electrochemical performance. This enhancement is primarily attributed to the synergistic effects of the binary nickel cobalt nitride composition and the porous nanosheet morphology. These factors significantly improved charge transfer kinetics, enhanced ion diffusion, and provided a large electroactive surface area. Comprehensive structural and chemical, including XRD, XPS, EDS, and FTIR analyses, confirmed the successful synthesis of NiCoN with the desired elemental composition and chemical states. The hierarchical architecture of the NiCoN electrode material facilitated efficient electron and ion transport, contributing to its excellent electrochemical characteristics, such as high specific capacitance, robust rate capability, and long-term cycling stability. In the practical application of the NiCoN//AC ASC device, it delivered an impressive energy density of 36 W h kg^{-1} at a power density of 775 W kg^{-1}, while maintaining 85% of its initial capacitance after 5000 charge–discharge cycles, highlighting its outstanding cycling stability and durability. Overall, this research offers valuable insights into the design and optimization of binary metal nitride-based electrodes, contributing significantly to the advancement of energy storage technologies. The findings pave the way for future exploration and innovation in high-performance ASCs and other energy storage devices.

Data availability

The original contributions presented in the study are included in the article, further inquiries can be directed to the corresponding author.

Author contributions

Mohan Reddy Pallavolu: methodology, conceptualization, investigation, data curation, writing – original draft, formal analysis, writing review; Chandu V. V. Muralee Gopi: writing – original draft, formal analysis, writing review – editing; Samikannu Prabu: review – editing; Punna Reddy Ullapu: software, formal analysis; Jae Hak Jung: editing, supervision; Sang Woo Joo: editing, supervision, resources, project administration, funding acquisition; R. Ramesh: funding acquisition and supervision.

Conflicts of interest

No known competing interest to declare in this paper.

Acknowledgements

The authors acknowledge the grant of 2019R1A5A8080290 from the National Research Foundation of Korea. Also, this work is supported by the Adama Science and Technology University.

References

1 M. Salanne, B. Rotenberg, K. Naoi, K. Kaneko, P.-L. Taberna, C. P. Grey, B. Dunn and P. Simon, *Nat. Energy*, 2016, **1**, 1–10.
2 K. Krishnamoorthy, P. Pazhamalai, V. K. Mariappan, S. S. Nardekar, S. Sahoo and S.-J. Kim, *Nat. Commun.*, 2020, **11**, 2351.
3 P. Cicconi and P. Kumar, *J. Energy Storage*, 2023, **73**, 109197.
4 Y. Chen, Y. Kang, Y. Zhao, L. Wang, J. Liu, Y. Li, Z. Liang, X. He, X. Li, N. Tavajohi and B. Li, *J. Energy Chem.*, 2021, **59**, 83–99.
5 K. Dissanayake and D. Kularatna-Abeywardana, *J. Energy Storage*, 2024, **96**, 112563.
6 A. K. Lichchhavi and P. M. Shirage, *J. Energy Storage*, 2022, **55**, 105692.
7 J. Zhang, M. Gu and X. Chen, *Micro Nano Eng.*, 2023, **21**, 100229.
8 L.-Q. Mai, A. Minhas-Khan, X. Tian, K. M. Hercule, Y.-L. Zhao, X. Lin and X. Xu, *Nat. Commun.*, 2013, **4**, 2923.
9 J. Acharya, B. G. S. Raj, T. H. Ko, M.-S. Khil, H.-Y. Kim and B.-S. Kim, *Int. J. Hydrogen Energy*, 2020, **45**, 3073–3085.
10 A. Acharjee and B. Saha, *J. Mol. Liq.*, 2024, **400**, 124487.
11 S. M. S. M. Rahat, K. Md. Z. Hasan, Md. M. H. Mondol and A. K. Mallik, *J. Energy Storage*, 2023, **73**, 108847.
12 M. Girirajan, A. K. Bojarajan, I. N. Pulidindi, K. N. Hui and S. Sangaraju, *Coord. Chem. Rev.*, 2024, **518**, 216080.
13 C. V. V. M. Gopi, R. Ramesh, R. Vinodh, S. Alzahmi and I. M. Obaidat, *Nanomaterials*, 2023, **13**, 1125.
14 M. S. Iyer and I. Rajangam, *J. Energy Storage*, 2023, **67**, 107530.
15 A. Asghar, K. Khan, O. Hakami, W. M. Alamier, S. K. Ali, T. Zelai, M. S. Rashid, A. K. Tareen and E. A. Al-Harthi, *Front. Chem.*, 2024, **12**, 1402563.
16 J. Zhao, S. Xu, K. Tschulik, R. G. Compton, M. Wei, D. O'Hare, D. G. Evans and X. Duan, *Adv. Funct. Mater.*, 2015, **25**, 2745–2753.
17 S. A. Kadam, R. S. Kate, V. M. Peheliwa, S. A. Shingate, C. C. S. Maria and Y.-R. Ma, *J. Energy Storage*, 2023, **72**, 108229.
18 B. Das, M. V. Reddy, P. Malar, T. Osipowicz, G. V. Subba Rao and B. V. R. Chowdari, *Solid State Ionics*, 2009, **180**, 1061–1068.
19 M.-S. Balogun, Y. Zeng, W. Qiu, Y. Luo, A. Onasanya, T. K. Olaniyi and Y. Tong, *J. Mater. Chem. A*, 2016, **4**, 9844–9849.
20 Y. Ruan, L. Lv, Z. Li, C. Wang and J. Jiang, *Nanoscale*, 2017, **9**, 18032–18041.
21 K. Li, B. Zhao, H. Zhang, H. Lv, J. Bai, H. Ma, P. Wang, W. Li, J. Si, X. Zhu and Y. Sun, *Adv. Funct. Mater.*, 2021, **31**, 2103073.
22 X. Liu, W. Zang, C. Guan, L. Zhang, Y. Qian, A. M. Elshahawy, D. Zhao, S. J. Pennycook and J. Wang, *ACS Energy Lett.*, 2018, **3**, 2462–2469.
23 F. Liu, L. Zeng, Y. Chen, R. Zhang, R. Yang, J. Pang, L. Ding, H. Liu and W. Zhou, *Nano Energy*, 2019, **61**, 18–26.
24 X. Gao, Y. Zhang, Y. Zhao, S. Yin, J. Gui, C. Sun and S. Guo, *Nano Energy*, 2022, **91**, 106701.
25 R. Kumar, *Nano-Micro Lett.*, 2020, **12**, 122.
26 D. Lee, Q. X. Xia, J. M. Yun and K. H. Kim, *Appl. Surf. Sci.*, 2018, **433**, 16–26.
27 N. Poompiew, P. Pattananuwat and P. Potiyaraj, *ACS Omega*, 2021, **6**, 25138–25150.
28 J. Lai, B. Huang, Y. Chao, X. Chen and S. Guo, *Adv. Mater.*, 2019, **31**, 1805541.
29 M. Irfan, I. U. Khan, J. Wang, Y. Li and X. Liu, *RSC Adv.*, 2020, **10**, 6444–6451.
30 S. Wang, L. Li, W. He, Y. Shao, Y. Li, Y. Wu and X. Hao, *Adv. Funct. Mater.*, 2020, **30**, 2000350.
31 K. Abdul Sammed, L. Pan, A. Farid, M. Javid, S. Yang and M. Asif, *ACS Appl. Energy Mater.*, 2021, **4**, 6678–6687.
32 G. Nagaraju, G. S. R. Raju, Y. H. Ko and J. S. Yu, *Nanoscale*, 2015, **8**, 812–825.
33 A. H. A. Rahim and S. R. Majid, *J. Appl. Electrochem.*, 2023, **53**, 1727–1737.
34 Y. Tang, Y. Liu, S. Yu, W. Guo, S. Mu, H. Wang, Y. Zhao, L. Hou, Y. Fan and F. Gao, *Electrochim. Acta*, 2015, **161**, 279–289.
35 Y. Matos-Peralta, D. Llanes, A. Cano, M. P. Hernández, L. Bazán-Bravo, F. Justo Chao Mujica, L. Felipe Desdín García, L. Reguera and M. Antuch, *ChemistrySelect*, 2022, **7**, e202201121.
36 M. Yan, Y. Yao, J. Wen, L. Long, M. Kong, G. Zhang, X. Liao, G. Yin and Z. Huang, *ACS Appl. Mater. Interfaces*, 2016, **8**, 24525–24535.
37 B. Cui, H. Lin, Y. Liu, J. Li, P. Sun, X. Zhao and C. Liu, *J. Phys. Chem. C*, 2009, **113**, 14083–14087.
38 X. Feng, H. Wang, X. Bo and L. Guo, *ACS Appl. Mater. Interfaces*, 2019, **11**, 8018–8024.
39 Y. Bu, J. Liu, D. Cai, P. Huang, S. Wei, X. Luo, Z. Liu, F. Xu, L. Sun and X. Wei, *J. Alloys Compd.*, 2023, **938**, 168495.
40 J. Liu, J. Wang, C. Xu, H. Jiang, C. Li, L. Zhang, J. Lin and Z. X. Shen, *Advanced Science*, 2018, **5**, 1700322.
41 W. Liu, X. Li, M. Zhu and X. He, *J. Power Sources*, 2015, **282**, 179–186.
42 S. Wu, X. Yang, T. Cui, Q. Feng, S. Zhou, X. Xu, H. Zhao, L. Wu, Y. He and Q. Yang, *Colloids Surf., A*, 2021, **628**, 127332.
43 M. Zhu, Q. Luo, C. Lu and L. Liu, *Appl. Organomet. Chem.*, 2024, **38**, e7354.
44 M. R. Thalji, G. A. M. Ali, J.-J. Shim and K. F. Chong, *Chem. Eng. J.*, 2023, **473**, 145341.
45 J. Zhao, Z. Li, X. Yuan, Z. Yang, M. Zhang, A. Meng and Q. Li, *Adv. Energy Mater.*, 2018, **8**, 1702787.
46 Y. Ouyang, X. Xia, H. Ye, L. Wang, X. Jiao, W. Lei and Q. Hao, *ACS Appl. Mater. Interfaces*, 2018, **10**, 3549–3561.
47 Q. Zong, H. Yang, Q. Wang, Q. Zhang, J. Xu, Y. Zhu, H. Wang, H. Wang, F. Zhang and Q. Shen, *Dalton Trans.*, 2018, **47**, 16320–16328.
48 P. Wen, P. Gong, J. Sun, J. Wang and S. Yang, *J. Mater. Chem. A*, 2015, **3**, 13874–13883.